PCCP

ROYAL SOCIETY OF CHEMISTRY

PAPER

Cite this: *Phys. Chem. Chem. Phys.*, 2021, **23**, 11863

First-principles study of the optical and thermoelectric properties of tetragonal-silicene†

Niladri Sekhar Mondal,[a] Subhadip Nath, *[b] Debnarayan Jana [c] and Nanda Kumar Ghosh[d]

Received 4th April 2021,
Accepted 26th April 2021

DOI: 10.1039/d1cp01466h

rsc.li/pccp

We report the optical and thermoelectric properties of the two-dimensional Dirac material T-silicene (TS) sheet and nanoribbons (NRs) by first-principles calculations. Both the optical and thermoelectric properties of TS can be modified by tailoring the sheet into nanoribbons of different widths and edge geometries. The optical response of the structures is highly anisotropic. A π interband transition occurs in the visible range of incident light with parallel polarization. The optical response for asymmetric armchair TS nanoribbons (ATSNRs) is larger than for symmetric ATSNRs. The absorptions of asymmetric ATSNR are redshifted due to a decrease in the bandgap with the width of the NRs. Plasma frequencies of the sheet and the NRs are identified from the imaginary part of the dielectric function and electron energy loss spectra curves. Thermoelectric properties like electrical conductivity, Seebeck coefficient, power factor, and electronic figure of merit are also studied. Compared with graphene, the TS sheet possesses a higher electrical conductivity and a better figure of merit. Among the NRs, asymmetric ATSNRs exhibit a better thermoelectric performance. All these intriguing features of TS may shed light on fabricating smart opto-electronic and thermoelectric devices.

1 Introduction

Recent years have seen incredible interest directed towards the experimental and theoretical study of two-dimensional (2D) materials with Dirac cones. Beginning with the eminent accomplishment of graphene,[1–5] the emphasis has additionally been on non-carbon-based 2D Dirac materials like silicene, germanene, stanene and so on.[6–8] Also, stable non-hexagonal allotropes of these materials possessing Dirac cone(s), like S-graphene (SG),[9,10] buckled tetragonal-silicene (TS)[11] and tetragonal-germanene (TGe),[12] *etc.*, have been proposed. In contrast to TS and TGe, the stable tetragonal graphene (TG) structure is planar with metallic behavior.[13] Apart from graphene or silicene, 2D heteroatomic structures consisting of both carbon and silicon atoms – silicon carbide (SiC)[14–16] structures – have also been predicted and the existence of such 2D structures in the form of grains in graphene oxide pores have been confirmed experimentally. Among the predicted SiC structures, the hexagonal form possesses a direct bandgap,[16] while the tetragonal SiC[17] has a single Dirac cone in its band structure.

The high optical transmission and absorption in the visible range have opened up the possibility of applications for graphene in photonics and opto-electronics,[18] although the zero bandgap feature of graphene reduces its prospect in practical applications. Nonetheless, the optical response of graphene nanoribbons (NRs) can be controlled by its edge and width modulation, leading to its suitability for opto-electronic devices.[19–21] Beyond the hexagonal form, square symmetric TG has been shown[22,23] to have optical absorption in the low- and high-energy regions for parallel and perpendicular polarization, respectively. Moreover, TG has been predicted to have potential prospects in gas sensing,[23,24] and non-linear optical devices[25] *etc.* Recently, Nath *et al.* have also reported the highly anisotropic optical response of another non-hexagonal graphene allotrope, the SG sheet and NRs.[26] The low-buckled silicene and germanene exhibit a bandgap opening higher than graphene due to spin–orbit coupling (SOC). Also, a band gap opening at Dirac point can be tailored by external functionalization.[27,28] It has also been established that only the low-buckling form of silicene is stable, while high-buckling and planar silicene structures are unstable.[29,30] The optical response of the silicene has been found to possess two intense peaks in the visible and ultra-violet (UV) regions arising due to the top π–π* band and σ band transitions respectively.[31,32] At the same time, silicene has a wonderful optical response in the visible to infra-red (IR) region[33] making it a

[a] *Department of Physics, Haldia Government College, Haldia-721657, India*
[b] *Department of Physics, Krishnagar Government College, Krishnagar-741101, India. E-mail: subha.31connect@gmail.com*
[c] *Department of Physics, University of Calcutta, 92 A. P. C. Road, Kolkata-700009, India*
[d] *Department of Physics, University of Kalyani, Kalyani-741235, India*

† Electronic supplementary information (ESI) available. See DOI: 10.1039/d1cp01466h

potential candidate in the present optical and opto-electronics industries. For heteroatomic structures like SiC, this has an optical response mainly in the visible range, though is greatly affected by the positions of the C and Si atoms.[16,17]

Another technological aspect of a material is its thermoelectric properties, which deal with the ability to directly convert heat into electricity or *vice versa*. Along with other phenomenological properties, graphene has an extremely high thermal conductivity,[34] though this reduces its efficiency as a decent thermoelectric material. Also, it has been shown that thermoelectric merit is not improved for doped graphene NRs.[35] On the other hand, silicene and germanene have a better thermoelectric performance than graphene,[36] and it is considered that a small bandgap in the system improves the thermoelectric merit. Besides, it is natural to focus on the thermoelectric properties of silicon- and germanium-based materials being compatible with current technology.

Though the prediction and synthesis of the non-hexagonal form of graphene have been plentiful, allotropes of silicene with non-hexagonal symmetry are quite scarce. Among the few, T-silicene (TS)[11] possesses square symmetry with two Dirac cones in its band structure and has zero negative phonon frequency. Tu *et al.*[37] have shown that the bandgap of the TS sheet can be modulated upon hydrogenation (passivated by hydrogen atoms), which may find its application in spintronic devices. Similar band tuning has also been predicted for silicene nanosheets passivated by hydrogen.[38] Very recently[39] studying the electronic properties of TS nanoribbons (TSNRs), the authors predicted the existence of multiple Dirac cones, finite band gaps in their band structures depending on the width and the edge states of the nanoribbons (NRs).

Inspired by the above results, we have extended our previous work[39] in determining the optical and thermoelectric properties of the TS sheet and TSNRs using first-principles calculations. We have organized the paper as follows. In the next section (Section 2), we discuss briefly the structures. Also, the methodology used for our calculation is presented. Then in the 'Optical properties' section (Section 3), we study the optical properties like the real and imaginary parts of dielectric the functions, electron energy loss spectra (EELS), absorption coefficients, *etc.* as a function of frequency for different optical polarizations. In the subsequent Section 4, we investigate transport properties such as the electrical conductivity and Seebeck coefficient of TS sheet and TSNRs as a function of the chemical potential and temperature. We have also estimated the figure of merit, which characterizes the thermoelectric value.

2 Model and methodology

The structure of the TS sheet, shown in Fig. 1(a), consists of 8-atoms per unit cell and exhibits square symmetry with a lattice constant a = 7.6074 Å. The two different bond lengths are 2.252 Å (l_1) and 2.302 Å (l_2), which are also schematically depicted in the figure. The structure has a buckling of $\Delta Z \approx 0.49$ Å. This silicon-based structure has a cohesive energy 4.58 eV per atom, which is slightly lower than silicene (4.77 eV per atom).[11] Moreover, the structure does not have any imaginary frequency in the phonon dispersion and is mechanically stable up to 1000 K. Also, the mechanical properties of this structure are comparable to silicene.[39] NRs with armchair edges (ATSNRs) and zigzag edges (ZTSNRs) of different widths are cut along *X*- and *XY*-axis (45° with the *X*-axes) respectively from the relaxed sheet as shown in Fig. 1(b–d). The ATSNRs can be divided into two groups, based on the symmetric (S-ATSNR) and asymmetric (A-ATSNR) opposite edges.

The optical properties are explored using the SIESTA DFT package[40–42] using the generalized gradient approximation (GGA) of the Perdew–Burke–Ernzerhof (PBE) functional.[43] A Troullier–Martins[44] norm-conserving pseudopotential in a fully separable form of Kleinman and Bylander is used for the calculations. The double ζ plus polarised (DZP) basis set is used for the whole range of the systems. The TS sheet is optimised using a 32 × 32 × 1 Monkhorst–Pack (MP)[45] with the forces on individual atoms below 0.001 eV Å^{-1}. NRs of different width and edge geometries (S-ATSNRs, A-ATSNRs, and ZTSNRs) are tailored from the optimized sheet, and the dangling bonds at the edges are passivated with hydrogen for stability purposes.

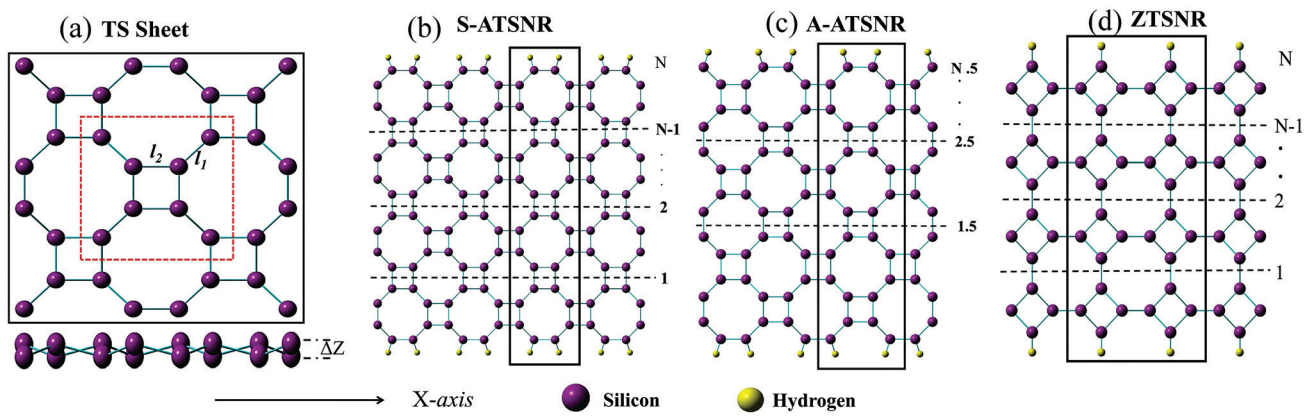

Fig. 1 (a) Optimized structure of TS with top and side views. The unit cell is marked with a red box, and the two different bonds l_1 and l_2 are shown. Structure of (b) S-ATSNR, (c) A-ATSNR and (d) ZTSNR. Unit cells for each NR are shown in black boxes, where *N* denotes the primitive unit cell of the TS.

The sheet is further optimized using a 32 × 1 × 1 MP with a force per atom below 0.01 eV Å^{-1}. For calculating the optical properties, the Brillouin zone (BZ) is sampled with a dense k space sampling with an equivalent of 151 × 151 × 1 and 151 × 1 × 1 Monkhorst–Pack (MP) for the sheet and nanoribbons respectively. A vacuum region of 15 Å is kept between two TS layers to avoid interaction between the neighboring layers. The mesh cutoff is set at 360 Ry.

It has already been established that the DZP basis set provides well-converged results in calculating the lattice parameter, Bulk modulus, and cohesive energy of bulk silicon.[42] However, to validate its applicability on the optical properties, we have computed the optical properties of bulk-silicon and silicene by DFT and compared them with a previous experimental and theoretical study (ESI†). In addition to the DZP basis set with PBE, we have considered a single ζ-polarised (SZP) and triple ζ-polarised (TZP) basis set. In the local density approximation (LDA) of the exchange–correlation, we have chosen the Perdew–Zunger[46] functional with the DZP basis set. Our DFT calculation of optical properties with the PBE/DZP level of theory gives good agreement with the experimental result of bulk-silicon (ESI Part-I†) and the theoretical result of silicene (ESI Part-II†). Since the PBE/DZP level of theory provides sensible results with an optimal computational cost for bulk silicon and silicene, it may be applied to any silicon-based structure to explore its optical properties including TS. Also, it is well known that DFT with various exchange functionals underestimates bandgap of bulk Si.[47,48] In this paper, we have used the band structure to illustrate the role of some important transitions between the valence band and conduction bands responsible for the peaks in the imaginary part of the dielectric function, and we believe that the GGA with the PBE functional and DZP basis provides reasonable good quality results with optimal computational cost.

The optical properties for all three directions have been calculated from the frequency (ω) dependent dielectric function $\varepsilon(\omega) = \varepsilon_1(\omega) + i\varepsilon_2(\omega)$, where $\varepsilon_1(\omega)$ and $\varepsilon_2(\omega)$ are the real and imaginary parts of the dielectric functions respectively. In the long-wavelength limit ($q \to 0$), using first-order time-dependent perturbation theory in the dipole approximation, the imaginary part of the dielectric function can be written as[49]

$$\varepsilon_2(q \to 0, \omega) = \frac{2e^2\pi}{\Omega\varepsilon_0} \sum_{K,CB,VB} \left|\langle \psi_K^{VB} | \vec{u} \cdot \vec{r} | \psi_K^{CB} \rangle\right|^2 \times \delta\left(E_K^{CB} - E_K^{VB} - \omega\right) \quad (1)$$

where Ψ_K^{CB} and Ψ_K^{VB} are the corresponding wave functions of the conduction band (CB) and valence band (VB) respectively at the K point, and Ω, ε_0, $\vec{u}$, and $\vec{r}$ represent the volume of the supercell, the free space permittivity, the polarization vector of the electric field, and the position vector respectively. The $\varepsilon_1(\omega)$ depends on $\varepsilon_2(\omega)$ *via* the Kramers–Kronig (KK) relation.[26]

Different optical properties like the absorption coefficient ($\alpha(\omega)$), electron energy loss spectra (EELS, ($L(\omega)$)) *etc.* have been calculated from the complex dielectric function for the *X*-, *Y*- and *Z*-directions. A large number of empty bands (N_{bands} = 500) have been considered with an optical broadening of 0.2 eV for more accurate results, due to the incorporation of high-frequency effects in interband transitions. The excitonic effect has not been considered in this work. We are keen on investigating the optical properties of the systems utilizing DFT as a computationally inexpensive method.

We have also calculated the effective number of the valence electrons (N_{eff}) in each unit cell[50] that contribute to the direct interband transitions using $\varepsilon_2(\omega)$ as a parameter given by the following sum rule

$$N_{eff}(\omega) = \frac{2m}{N_0 h^2 e^2} \int_0^{\omega_m} \omega\varepsilon_2(\omega) d\omega \quad (2)$$

Here m, e, h, N_0, ω and ω_m are the mass, the charge of the electrons, Planck's constant, the electron density, the energy, and the upper limit of the energy in eV.

The effective dielectric function ε_{eff}, which is determined by an interband and low-lying transition among the core and semi-core bands in the same range, can be expressed as

$$\varepsilon_{eff}(\omega) = 1 + \frac{2}{\pi} \int_0^{\omega_m} \omega^{-1}\varepsilon_2(\omega) d\omega \quad (3)$$

The effective dielectric function determines the most important contribution of the transitions to the static dielectric function in the energy range 0 (zero) to ω_m.

The EELS function has been calculated from the complex dielectric function as

$$L(\omega) = \mathrm{Im}\left(-\frac{1}{\varepsilon(\omega)}\right) = \frac{\varepsilon_2}{\varepsilon_1^2 + \varepsilon_2^2} \quad (4)$$

The peak position of the EELS can be used to estimate the total energy of the plasmons. A peak in EELS is obtained when $\varepsilon_1(\omega) \to 0$ and $\varepsilon_2(\omega) < 1$.

The optical absorption coefficient ($\alpha(\omega)$) is related to the imaginary part of the refractive index (extinction coefficient, $k(\omega)$) by the equation

$$\alpha(\omega) = \frac{2k\omega}{c\hbar} \quad (5)$$

where the complex refractive index has been calculated from the dielctric function using $\tilde{N}(\omega) = n(\omega) + ik(\omega) = \sqrt{\varepsilon(\omega)}$. The parameters $n(\omega)$ and $k(\omega)$ are related to ε_1 and ε_2 as

$$n(\omega) = \left(\frac{\sqrt{\varepsilon_1^2 + \varepsilon_2^2} + \varepsilon_1}{2}\right)^{\frac{1}{2}} \quad (6)$$

$$k(\omega) = \left(\frac{\sqrt{\varepsilon_1^2 + \varepsilon_2^2} - \varepsilon_1}{2}\right)^{\frac{1}{2}} \quad (7)$$

The thermoelectric properties of the TS sheet are calculated using the QUANTUM ESPRESSO (QE)[51,52] package with plane-wave basis[48,49] and the Boltzmann transport equation (BTE) with the relaxation time approach as implemented in the BoltzTraP code.[53] The BoltzTraP code uses the constant relaxation time approximation and rigid band approximation for the

solution of the BTE. For the input of the BTE solver, we perform spin unpolarised simulation with a Projected Augmented Wave technique (PAW), with the GGA in the shape of the PBE to approximate the exchange–correlation energy as executed in the QE package. The kinetic energy cutoff for charge density and wave function are taken as 600 Ry and 50 Ry respectively, and the BZ integration is performed by using a dense $24 \times 24 \times 1$ and $24 \times 1 \times 1$ k point mesh[45] for the sheet and nanoribbons respectively. In all calculations, we used the Gaussian smearing technique with a width of 0.005 Ry. A vacuum region of more than 15 Å is kept between the TS layers to avoid interaction between neighboring layers. The geometries of the sheet and hydrogen passivated nanoribbons are optimized until the forces in each atom are less than 0.01 eV Å^{-1}. The convergence for kinetic energy cutoff, k-grid points, is checked by calculating the total energy and formation energy of the TS sheet and is compared with earlier results. We have also calculated the formation energy and bandgap of bulk silicon using this same technique and found the results to be consistent with the experimental value.

The electrical conductivity ($\sigma_{\alpha\beta}$), Seebeck coefficient ($S_{\alpha\beta}$) and electronic thermal conductivity ($\kappa^{e}_{\alpha\beta}$) tensors are the important transport properties calculated by the code. These quantities are approximated in terms of temperature (T) and chemical potential (μ) as:[53]

$$\sigma_{\alpha\beta}(T,\mu) = \frac{1}{\Omega}\int \sigma_{\alpha\beta}(\varepsilon)\left[-\frac{\partial f_{\mu}(T,\varepsilon)}{\partial \varepsilon}\right]\mathrm{d}\varepsilon \tag{8}$$

$$S_{\alpha\beta}(T,\mu) = \frac{1}{eT\sigma_{\alpha\beta}(T,\mu)}\int \sigma_{\alpha\beta}(\varepsilon)(\varepsilon-\mu)\left[-\frac{\partial f_{\mu}(T,\varepsilon)}{\partial \varepsilon}\right]\mathrm{d}\varepsilon \tag{9}$$

$$\kappa^{e}_{\alpha\beta}(T,\mu) = \frac{1}{\Omega e^2 T}\int \sigma_{\alpha\beta}(\varepsilon)(\varepsilon-\mu)^2\left[-\frac{\partial f_{\mu}(T,\varepsilon)}{\partial \varepsilon}\right]\mathrm{d}\varepsilon \tag{10}$$

with

$$\sigma_{\alpha\beta}(\varepsilon) = \frac{e^2}{N}\sum_{i,k}\tau_{i,k}v_{\alpha}(i,k)v_{\beta}(i,k)\delta\left(\varepsilon-\varepsilon_{i,k}\right) \tag{11}$$

where α and β represent the tensor indices. The symbols $\varepsilon(k)$, $v(k)$, $\tau(k)$, f, e and Ω represent the band energy, band velocity, relaxation time, Fermi function, electronic charge and volume of the cell respectively.

The thermoelectric performance of a material is defined in terms of its figure of merit (ZT), a dimensionless quantity, expressed as follows:

$$ZT = \frac{\sigma S^2 T}{\kappa_{\mathrm{el}}+\kappa_{\mathrm{ph}}} = \frac{\sigma S^2 T}{\kappa_{\mathrm{el}}}\left(\frac{1}{1+\kappa_{\mathrm{ph}}/\kappa_{\mathrm{el}}}\right) = \frac{ZT_{\mathrm{el}}}{1+\kappa_{\mathrm{ph}}/\kappa_{\mathrm{el}}} \tag{12}$$

where $ZT_{\mathrm{el}} = \sigma S^2 T/\kappa_{\mathrm{el}}$ is the electronic figure of merit, and describes the upper bound of the total figure of merit. κ_{el} and κ_{ph} are electronic and phononic contributions of thermal conductivity.

Within the constant relaxation time approximation, the Seebeck coefficient and figure of merit can be calculated independently of the relaxation time (τ) but the evaluation of the electrical conductivity as well as the electronic thermal conductivity requires knowledge of τ. As a result, τ has been set as a fixed parameter to look for the variation of all the transport properties with temperature.

3 Optical properties

It is well established that the optical properties of the system strongly depend on the electronic properties. The electronic properties of the TS sheet and the NRs were explored in ref. 39. The band structure of the TS sheet possesses two Dirac cones in the irreducible Brillouin zone. S-ATSNRs exhibit multiple Dirac cones in their band structure depending on the width of the NRs, while A-ATSNRs are semiconductors. The ZTSNRs are also degenerate semiconductors with the existence of Dirac-like cones.

We have calculated the optical properties of the systems from the frequency-dependent complex part of the dielectric function $\varepsilon_2(\omega)$ under the condition of polarized light. We have considered the electric field parallel and perpendicular to the samples on the X–Y plane. We denote E_x (E_y) for parallel polarization along X- (Y-) direction, while E_z represents perpendicular polarization. For the sheet, both E_x and E_y are equivalent due to the symmetry of the structure, and hence conveniently we show the results for E_x only. In general, the optical response of the TS system is seen to be in the infrared (IR) to UV region (0–6 eV) and the UV region (6–15 eV) for light incidence with parallel and perpendicular polarizations respectively. Since the response for perpendicular polarization is in the UV region, we mainly study the optical properties for parallel polarization for the NRs unless otherwise stated. The anisotropy in the dielectric function arises due to the two-dimensional nature of the TS sheet.

3.1 Imaginary part of dielectric functions

3.1.1 TS sheet. Before discussing the optical properties of TS structures, we first check the convergence behavior of the PBE/DZP level of theory by calculating the imaginary part of the dielectric function $\varepsilon_2(\omega)$ for parallel and perpendicular polarization (Fig. 2a and b respectively) using the PBE/DZP, PBE/SZP, PBE/TZP and PZ/DZP levels of theory. A good convergence of $\varepsilon_2(\omega)$ is achieved for PBE/DZP with the PBE/TZP level of theory for both polarizations. Since all other optical properties are calculated from this imaginary part of the dielectric function, we can consider only the DZP basis with the PBE functional of the GGA exchange–correlation for our study.

The imaginary part of the dielectric function $\varepsilon_2(\omega)$, which measures the amount of energy dissipated in the system with frequency, shows two intense peaks with maxima at ω = 1.32 eV and 4.32 eV appears for parallel polarization (E_x) irrespective of the choice of the basis set and functional. The low energy peak (A) at 1.32 eV arises due to the interband transition from the VB to CB, arising due to π–π* sp-hybridized electrons. The high energy peak (B) arises due to the σ–σ* transition in the band structure. The peaks of the $\varepsilon_2^x(\omega)$ can be well explained in terms of the DOS and band structure of the TS. It is clear from the

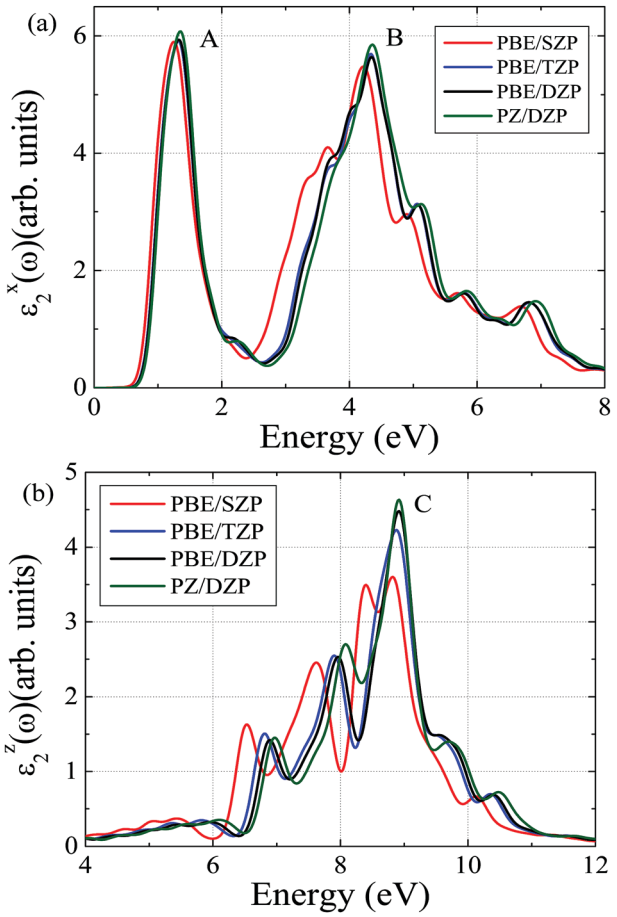

Fig. 2 Imaginary part of dielectric function $\varepsilon_2(\omega)$ for incidence of light with (a) parallel polarization and (b) perpendicular polarization with different levels of theory.

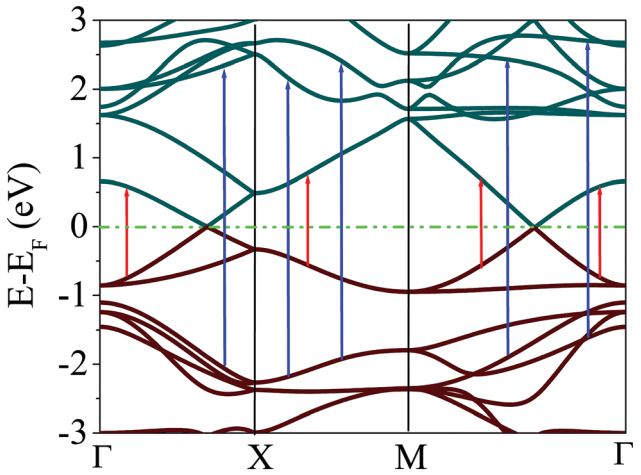

Fig. 3 Transitions for the peak 'A' at ω = 1.32 eV (red arrows) and a few of the possible transitions for peak 'B' at ω = 4.32 eV (blue arrows) are shown using the band structure of TS. The transitions are shown for the PBE/DZP level of theory.

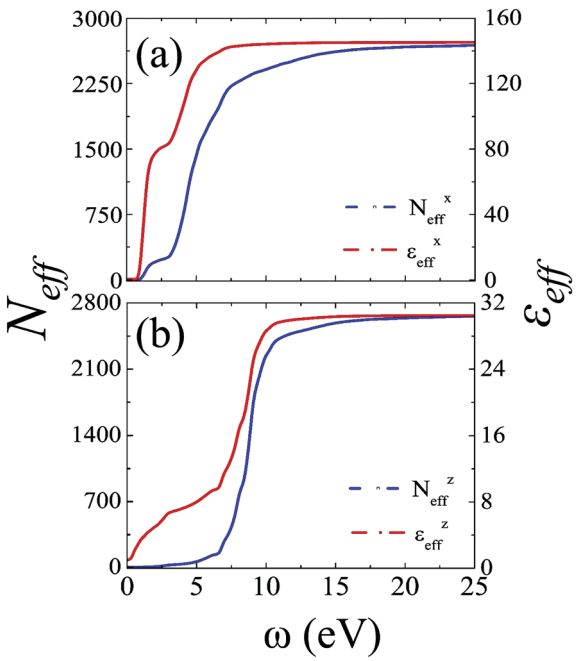

Fig. 4 Effective number of electrons (blue lines) and effective optical dielectric function (red lines) for the TS sheet as a function of energy for (a) E_x and (b) E_z.

DOS that the p_z orbital only contributes to the band structure near the Fermi level (E_F).[39] The interband transitions for the peaks at ω = 1.32 eV and 4.32 eV are shown in Fig. 3 with the band structure of the TS sheet. Four possible transitions at different K points between the highest VB and lowest CB contribute to peak 'A'. The few possible transitions for the peak 'B' arise from the bands deep in the VB and CB.

For perpendicular polarization (E_z), the $\varepsilon_2^z(\omega)$ shows a response in the region of 7–10 eV. A single intense peak (C) is observed at 8.88 eV, associated with some small peaks in the low energy region. The peak(s) arise due to σ–σ* band transitions. The few of the possible transitions leading to peak 'C' at 8.88 eV are shown with the band structure in the ESI,† Fig. S5. All these peaks arise as the number of transitions is large at these energy values compared with its vicinity.

The variation of N_{eff} (expressed in the unit of $\frac{2m}{N_0 h^2 e^2}$) and $\varepsilon_{\text{eff}}(\omega)$ with energy for E_x and E_z are shown in Fig. 4(a and b) respectively. For E_x, the $\varepsilon_{\text{eff}}(\omega)$ is nearly equal to unity up to $\omega \approx 0.6$ eV and then increases rapidly and reaches saturation at $\omega \approx 7.0$ eV. The rapid increase occurs between 0.6 and 5 eV, which suggests that the maximum contribution from the interband transition occurs between 0.6 and 5 eV. However, for E_z the saturation region is obtained at $\omega \approx 11$ eV, with a sharp rise for ω between 5 and 10 eV. This is the direct consequence of the interband transition within the σ–σ* band transition, which generally lies in the UV range. The plot of N_{eff} with energy indicates a saturation region at $\omega \approx 20$ eV for E_x. Thus it can be concluded that deep-lying valence electrons lying far from E_F do not contribute significantly in the optical transition with parallel polarization. For E_z, the saturation region occurs even at lower energy $\omega \approx 15$ eV. Interestingly, for perpendicular

polarization N_{eff} is very small in the region ω = 1–6 eV, which suggests that the electrons are not at all excited at small energy values for perpendicular polarization.

3.1.2 Nanoribbons

Polarization along the X-axis. We now present the variation of $\varepsilon_2(\omega)$ for all TSNRs with different widths (N = 1–4) for parallel polarization along the X-direction, in Fig. 5(a). For all S-ATSNRs, a peak is observed around $\omega \approx 1$, except for N = 1. The maximum in $\varepsilon_2^x(\omega)$ is observed for N = 2 at at $\omega \approx 0.94$ eV, which is blue-shifted with the increase in width. For N = 3 and 4, the peak in $\varepsilon_2^x(\omega)$ occurs at $\omega \approx 1.06$ and 1.12 eV respectively. Also, the maximum value decreases with the increase in the width. The peak occurs due to the transition in the π–π* band in the band structure. Additionally, a moderate optical response is observed at 3.8–5 eV for all N values under study, which can be attributed to the π–σ* transition. Contrary to the above findings, the width N = 1 has the maximum around $\omega \approx$ 4.80 eV with no optical response in the IR to the visible region.

Compared with S-ATSNR, the intensities of the peaks are very large for A-ATSNR and increase with the width. Additionally, the peak positions are red-shifted with the increase in the width. This result is a direct consequence of the decrease in the bandgap of A-ATSNR with width. Moreover, for A-ATSNR the optical response is observed in the IR region of the EM spectrum.

The width-dependent variation of $\varepsilon_2^x(\omega)$ for ZTSNRs is quite irregular. A small optical response for the narrowest ZTSNR is observed in the UV region only with a peak at 4.26 eV. However, for $N \geq 2$, a strong response in both the IR to visible region is observed along with a weak response in the UV region. For the even N, the peak in the IR region is red-shifted while for odd N the peak is blue shifted. In the UV region, the peaks for all ZTSNRs are observed around $\omega \approx 4.5$ eV.

Polarization along the Y-axis. The dependency of $\varepsilon_2(\omega)$ on ω for polarization of light along E_y, for all types of TSNRs, is shown in Fig. 5(b). Both S-ATSNR and A-ATSNR show similar behavior in $\varepsilon_2^y(\omega)$ with ω. However, the peak intensity of $\varepsilon_2^y(\omega)$ for S-ATSNR is large compared to $\varepsilon_2^x(\omega)$. The intensity of the optical response is proportional and is red-shifted towards smaller frequencies with the increase of width. For example, the peak positions are observed at ω = 0.94, 0.78, and 0.68 eV for S-ATSNR while for A-ATSNR they are at ω = 1.02, 0.86 and 0.70 eV for N = 2, 3, 4 respectively. The narrowest NRs show a negligible optical response, which can be attributed to the confinement effect.

The ZTSNRs show a weaker response compared with the S-ATSNRs and A-ATSNRs. However similar to the other two NRs, the peak height increases with width and is red-shifted. Contrary to the other two NRs, N = 2 and 3 shows a response in the IR to visible region of the EM spectrum. The peak positions for N = 2–5 are at ω = 1.7, 1.18, 1.04 and 0.88 eV respectively.

Polarization along the Z-axis. For perpendicular polarization, the optical response of all TSNRs is observed in the UV region *i.e.* at 7–11 eV and is depicted in Fig. 5(c). The most intense peak for all NRs and widths is observed around $\omega \approx 8.9$ eV. These peaks are related to the σ–σ* band transitions.

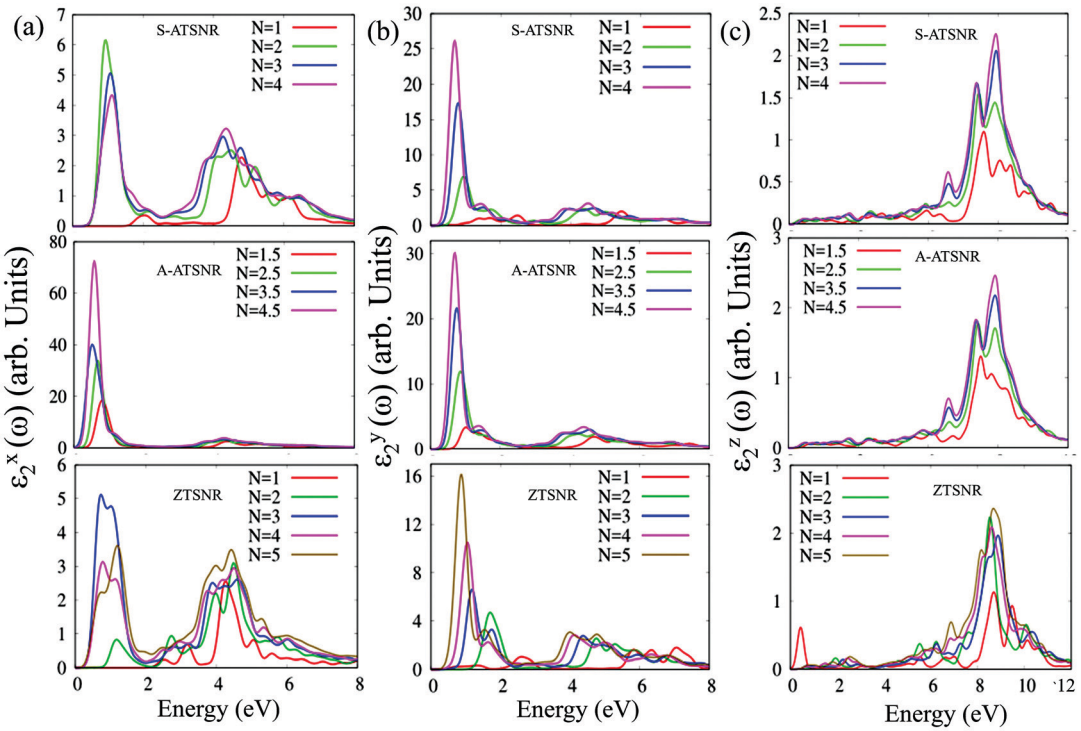

Fig. 5 Imaginary part of the dielectric function for polarization along the (a) X-axis (first column) (b) Y-axis (second column) and (c) Z-axis (third column). The top panel is for S-ATSNR, the middle for A-ATSNR and the bottom panel for ZTSNR.

A few small peaks are also observed other than the maximum intensity peaks.

3.2 Real part of dielectric functions and EELS

The real part of the dielectric function $\varepsilon_1(\omega)$ measures the amount of energy stored in the system. In the metallic system, it plays an important role in determining the collective role of free electrons. A rapid fluctuation is observed in $\varepsilon_1(\omega)$ at each peak in $\varepsilon_2(\omega)$. The real part of the dielectric function along with electron energy loss factor (EELS) for the sheet and different NRs are discussed in the following subsection.

3.2.1 TS sheet. The real part of the dielectric function for the TS sheet is shown in Fig. 6(a). Our study reveals that the static part of the dielectric function is $\varepsilon_1^x(0) = 3.9$ and $\varepsilon_1^z(0) = 1.60$ for polarization along the *X*- and *Z*-directions respectively. These values are comparable to free-standing silicene where $\varepsilon_1^x(0) = 5.43$ and $\varepsilon_1^z(0) = 1.47$.[33] The availability of a large number of free carriers in the TS sheet, which behaves like a semimetal, results in a non-zero value of $\varepsilon_1(0)$. The behavior of a material as a metal or a dielectric can be well understood by calculating the plasma frequency. It is the characteristic frequency, corresponding to the collective excitations of electrons, at which the real part of the dielectric function vanishes with $\varepsilon_1(\omega)$ evolving from negative to positive *i.e.* at $\varepsilon_1(\omega) = 0$. Few plasma frequencies (ω_p) are observed for both incidences along the *X*- and *Z*-axes. The plasma frequencies for incidence along parallel polarization are $\omega_p^x = 5.65$, 6.07, and 7.49 eV, while for perpendicular polarization $\omega_p^z = 10.15$ eV. The values of the plasma frequencies are tabulated in Table 1. Thus all the plasma frequencies for both polarizations appear in the UV region. The existence of plasma frequency from the real part of the dielectric function can well be verified from the EELS curve (shown in Fig. 6(b)), which shows a sharp peak at the plasma frequency. The sharpest plasmon peak in EELS for parallel polarization occurs at 7.64 eV and with a few small humps at 5.58 and 6.16 eV, in good agreement with the plasma frequencies. These peaks originate due to the loss of energy by fast-moving electrons in non-magnetic materials. Two prominent peaks of $\varepsilon_1^x(\omega)$ at 0.94 and 3.16 eV (visible region) occur for polarization along the *X*-direction. Three small peaks are observed for $\varepsilon_1^z(\omega)$ in the range of 6–9 eV.

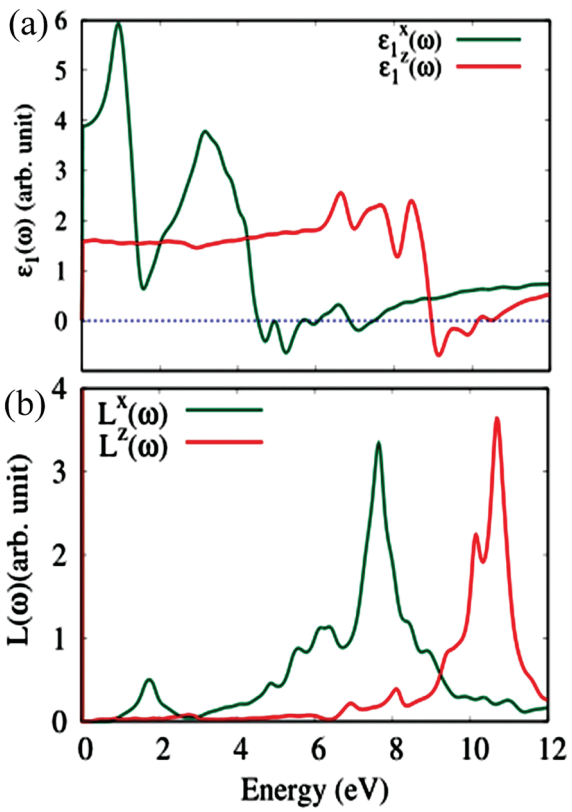

Fig. 6 (a) Real part of the dielectric function $\varepsilon_1(\omega)$ and (b) EELS ($L(\omega)$) for polarization along the *X*- and *Z*-axes for the TS sheet. The green curve is for parallel polarization and the red curve is for perpendicular polarization.

Table 1 Predicted plasma frequency ω_p of different structures

Structure	ω_p for polarization along *X* axis	ω_p for polarization along *Y* axis
TS sheet	5.65, 6.07 and 7.49	—
S-ATSNR-1	—	
S-ATSNR-2	1.58 and 5.54	1.20
S-ATSNR-3	1.46	1.90
S-ATSNR-4	5.53	1.94 and 5.50
A-ATSNR-1.5	1.94	—
A-ATSNR-2.5	2.12, 5.55 and 6.8	1.44
A-ATSNR-3.5	2.20, 4.94, 5.86 and 7.26	1.92 and 7.22
A-ATSNR-4.5	2.42 and 7.6	2.04 and 5.60
ZTSNR-1	—	7.70
ZTSNR-2	4.92	2.29
ZTSNR-3	1.58 and 5.27	2.13
ZTSNR-4	5.12	1.50, 1.90, 5.50 and 7.20
ZTSNR-5	5.58	1.34, 2.00 and 5.36

3.2.2 Nanoribbons

Polarization along the X-axis. The real part of the dielectric function of the nanoribbons for E_x is shown in Fig. 7(a). It is clear from the figure that the static part of the dielectric function $\varepsilon_1^x(0)$ for the A-ATSNR is larger than S-ATSNR and Z-ATSNR. The typical values of $\varepsilon_1^x(0)$ for the NRs of different widths are given in Table 2. One of the reasons for the large value of the static dielectric function for A-ATSNR may be due to the asymmetry in the structure. The plasma frequency for all the TSNRs for polarization along the *X*-direction is tabulated in Table 1. The low energy plasma frequency for A-ATSNR is blue-shifted with an increase in width. EELS peaks for all TSNRs match well with the plasma frequency. While the EELS peak for S-ATSNR is red-shifted, it is blue-shifted for A-ATSNR. Moreover, the EELS peak for A-ATSNR for $N = 1$ is very intense compared with other peaks. For ZTSNR, an intense peak is observed only for $N = 3$.

Polarization along the Y-axis. The variation of $\varepsilon_1(\omega)$ for E_y with frequency for all TSNRs is depicted in Fig. 8(a). It is clear from the figure that the static part of the dielectric function $\varepsilon_1(0)$ is larger for E_y than E_x, except for A-ATSNR. However, for all types of TSNRs, $\varepsilon_1^y(0)$ increases with the increase of the width. The typical values of $\varepsilon_1^y(0)$ are tabulated in Table 3. The obtained plasma frequencies are also listed in Table 1. The data indicate

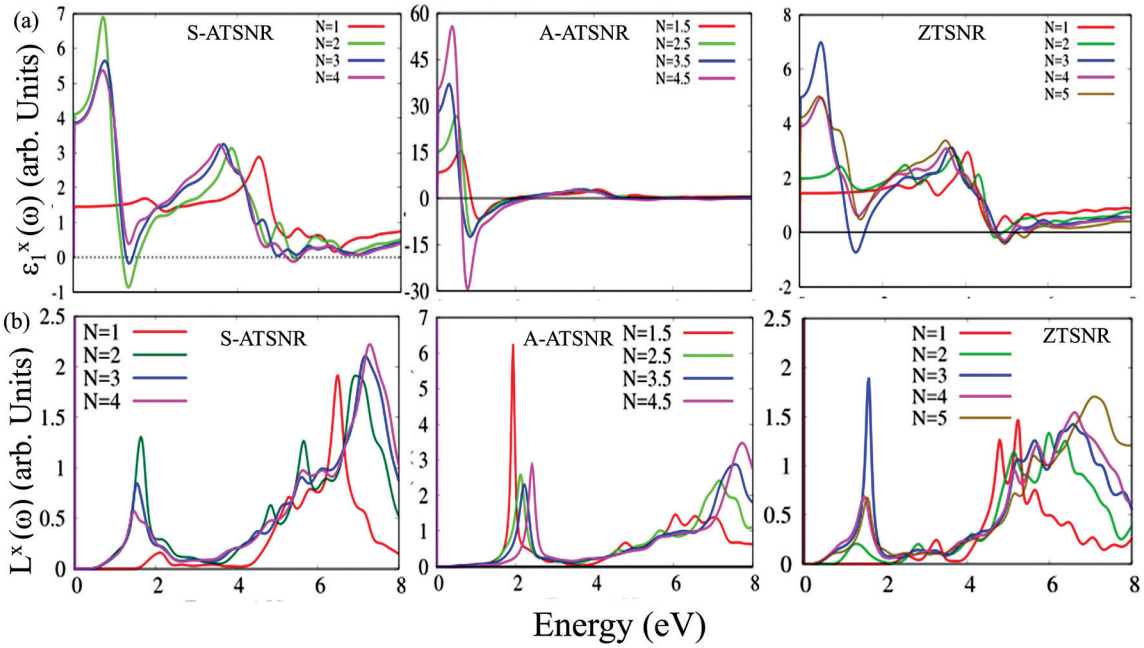

Fig. 7 (a) Real part of the dielectric function and (b) EELS for polarization along the *X*-axis for different TSNRs.

Table 2 Static dielectric function $\varepsilon_1^x(0)$ for S-ATSNR, A-ATSNR and ZTSNR for different widths for polarization along the *X*-axis

Width *N*	S-ATSNR	A-ATSNR	ZTSNR
1/1.5	1.45	8.39	1.44
2/2.5	4.11	15.29	1.98
3/3.5	3.86	28.03	4.97
4/4.5	3.83	35.43	3.90

that all the NRs exhibit plasma frequency in the visible range, which is further confirmed by the EELS peaks in Fig. 8(b). Both $\varepsilon_1(\omega)$ and EELS curves show that a few plasma frequencies also lie in the deep UV region.

3.3 Absorption co-efficient

The absorption co-efficient $\alpha(\omega)$ for polarization E_x and E_z for the TS sheet is shown in Fig. 9(a). The maximum value of $\alpha(\omega)$

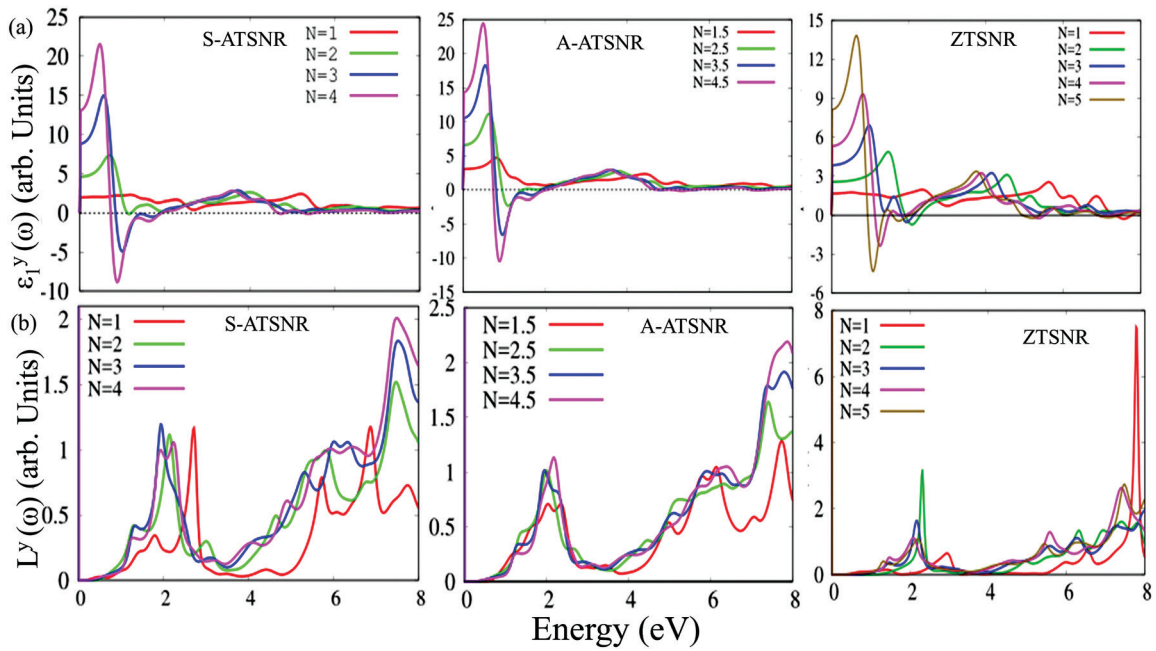

Fig. 8 (a) Real part of the dielectric function and (b) EELS for polarization along the *Y*-axis for different TSNRs.

Table 3 Static dielectric function $\varepsilon_1^y(0)$ for S-ATSNR, A-ATSNR and ZTSNR for different widths for polarization along the *Y*-axis

Width *N*	S-ATSNR	A-ATSNR	ZTSNR
1/1.5	1.96	3.04	1.65
2/2.5	4.60	6.56	2.55
3/3.5	8.83	10.56	3.84
4/4.5	13.07	14.33	5.32

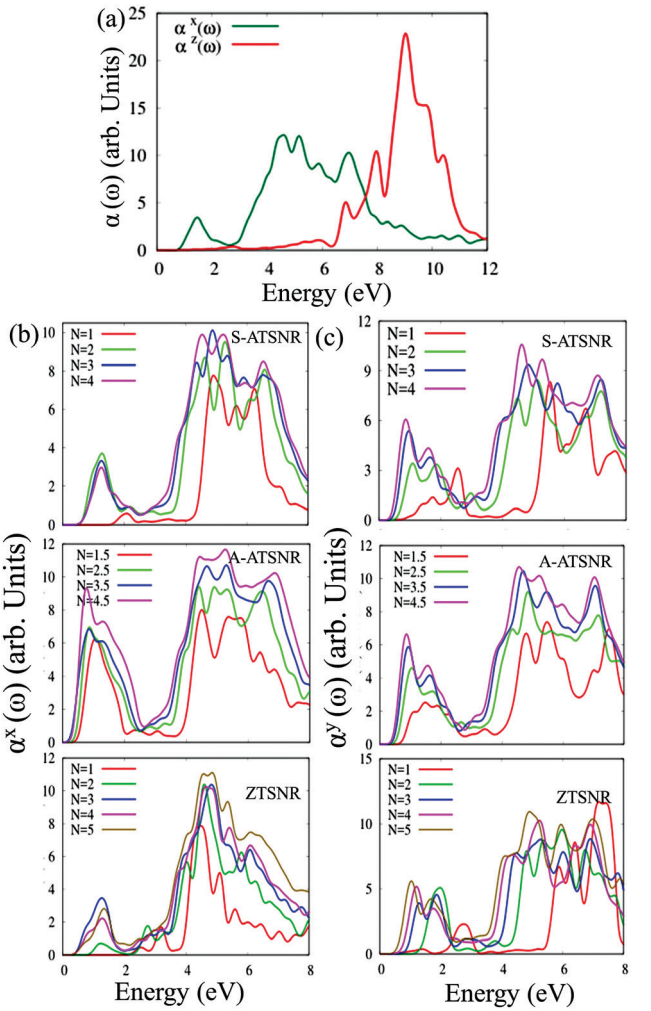

Fig. 9 Absorption coefficient for (a) polarization along the *X*- and *Z*-axes for the TS sheet, (b) and (c) for different TSNRs for polarization along the *X*- and *Y*-axes respectively.

for E_x is 12.15 and 12.05 at energy 4.60 and 5.16 eV, which is in the UV region. The maximum of $\alpha(\omega)$ for E_z is 22.83 at energy 9.02 eV, which lies deep in the UV region. The energy for maximum absorption is blue-shifted compared with pristine silicene (ω = 4.07 eV for α_x^{max}) for parallel polarization while it nearly matches that for perpendicular polarization (ω = 9.11 eV).[54] For the TSNRs (Fig. 9(b and c)), polarization of incident light along the *X*- and *Y*-axes shows strong absorption in the IR region ($\omega \approx$ 1–1.5 eV) and the UV region. However, the absorption in the UV region is stronger compared with the IR region. Generally, the

Table 4 Comparison of the static dielectric constant $\varepsilon_1(0)$, plasma frequency (ω_p) and the energy of absorption maximum (ω_α) for graphene, silicene and tetragonal-silicene (TS). *x* and *z* denote the incidence of light with parallel and perpendicular polarization

Optical properties	Graphene[33]	Silicene[33,54]	T-silicene [this work]
$\varepsilon_1^x(0)$	2.67	5.43	3.9
$\varepsilon_1^z(0)$	1.15	1.47	1.60
ω_p^x (in eV)	—	4.86	7.64[a]
ω_p^z (in eV)	—	—	10.15[a]
ω_α^x (in eV)	4.17	4.07	4.60
ω_α^z (in eV)	14.5	9.11	9.02

[a] Represents the maximum of the EELS peak.

absorption intensity increases with the width of the TSNRs and is redshifted. It is well established that the interband transition is mainly responsible for the absorption spectra peaks. With the increase in width, the bands are closely spaced, and hence the absorption can happen at low energies and hence is red-shifted. Irrespective of the width and the direction of the polarization of light, a very low value of the absorption coefficient is observed beyond the incident energy range ω = 10 eV. The large absorption co-efficient of ATSNRs in the IR and UV range may lead to its application in solar cells.

We finally compare the optical properties of the TS sheets in terms of the static dielectric constant, plasma frequency, and energy of absorption maximum (ω_α) with silicene and graphene and this is tabulated in Table 4. The values are quite comparable to silicene and graphene and in some cases they are better.

4 Thermoelectric properties

In a material, both charge and heat are transported by electrons. The electric field produced by the temperature gradient in any material opposes the natural diffusion of electrons. Thermoelectric energy conversion is the ability of a material to convert a steady temperature gradient into an electric current or *vice versa*. The thermoelectric properties of a material depend on its electronic structure. A small bandgap and higher carrier mobility are the prime requisite of good thermoelectric materials. Besides, functionalization and chemical potential also play a pivotal role in determining the thermoelectric properties. TS has two Dirac cones in the band structure (shiowing semi-metal behavior) and is expected to be a good thermoelectric material. The performance of TS as a thermoelectric material has been considered by studying various parameters like the electrical and thermal conductivity, Seebeck coefficient, power factor, and the figure of merit as a function of temperature and chemical potential. These results are depicted in Fig. 10. Also, we have plotted these thermoelectric parameters with temperature for arbitrary values of $\mu - \varepsilon_f$ for a better understanding of the temperature dependency of the thermoelectric performance. The relaxation time constant is assumed to be isotropic and constant in all directions. The pristine condition is represented by μ = 0 and $\mu > 0$ ($\mu < 0$) indicates the electron (hole) doping.

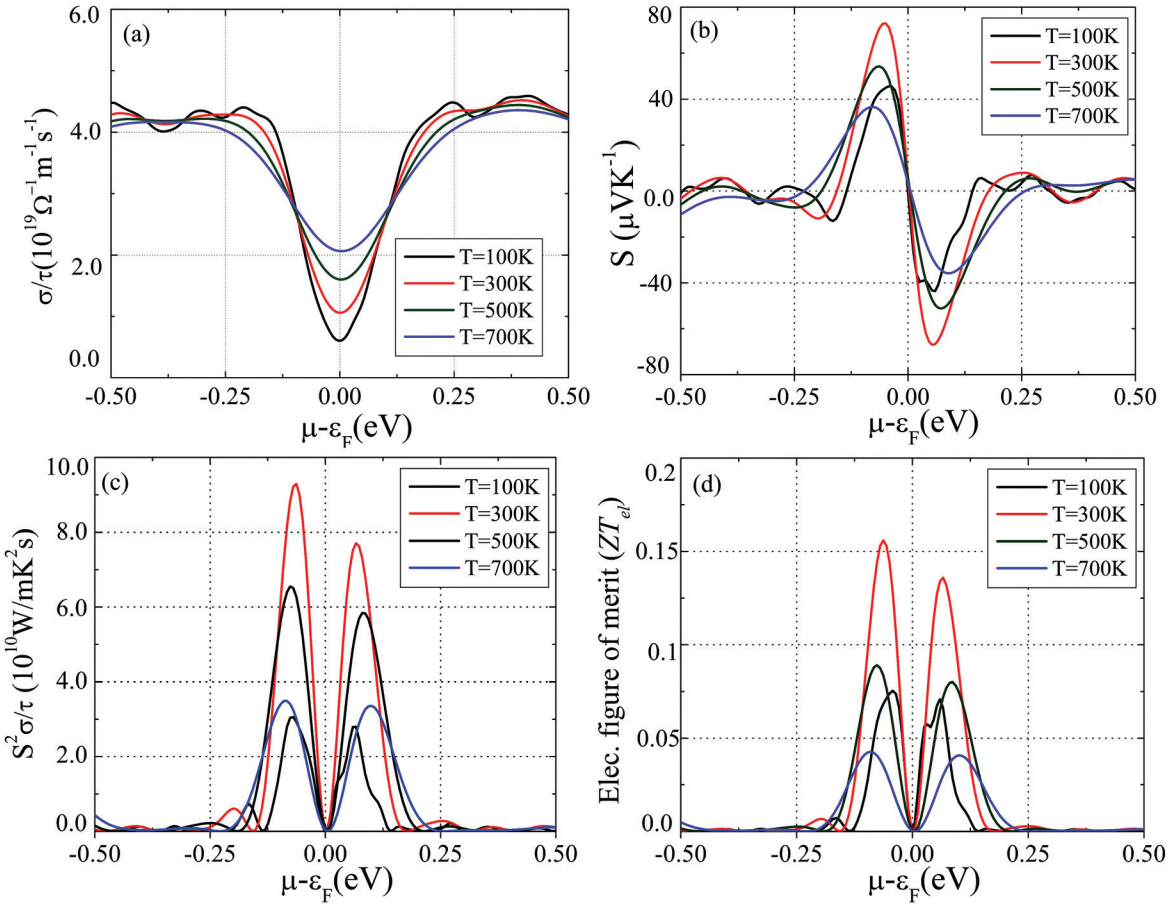

Fig. 10 Variation of the (a) electrical conductivity, (b) Seebeck coefficient, (c) power factor, and (d) electronic figure of merit with respect to the chemical potential.

4.1 TS sheet

The electrical conductivity σ/τ, which measures the ability of materials to conduct electricity, shows a nearly symmetric behavior around the chemical potential $\mu \rightarrow \varepsilon_f$ at all temperatures and tends to saturate at a higher temperature and chemical potential (Fig. 10a). As expected, the electrical conductivity tends to increase with temperature due to the formation of electron–hole pairs. For example, the $\sigma/\tau \approx 2.06 \times 10^{19}\ \Omega^{-1}\ m^{-1}\ s^{-1}$ and $6.12 \times 10^{18}\ \Omega^{-1}\ m^{-1}\ s^{-1}$ at 700 K and 100 K respectively for $\mu \rightarrow \varepsilon_f$. However, for the doped systems the electrical conductivity is higher than the pristine system due to the injection of charge carriers by doping (Fig. S6(a), ESI†). At room temperature, the maximum of the electrical conductivity $4.52 \times 10^{19}\ \Omega^{-1}\ m^{-1}\ s^{-1}$ appears at $\mu - \varepsilon_f = 0.40$ eV. The DOS shows a symmetric nature in the VB and CB around the Fermi surface,[39] which suggests equal carrier concentrations around the VB and CB edge. This implies a nearly symmetric behavior of the electrical conductivity around $\mu - \varepsilon_f = 0$.

The variation of the Seebeck coefficient (S) with the chemical potential (μ) is shown in Fig. 10b. The sign of the Seebeck coefficient indicates the nature of the majority carriers (electrons/holes) for the system with $\mu - \varepsilon_f \neq 0.0$. It is evident from the figure that the Seebeck coefficient reaches a minimum ($-67.0 \times 10^{18}\ \mu V\ K^{-1}$) at $\mu - \varepsilon_f = 0.053$ eV (this corresponds to the maximum value of the Seebeck coefficient for electron doping), while it reaches the maximum value ($72.7 \times 10^{18}\ \mu V\ K^{-1}$) at $\mu - \varepsilon_f = -0.056$ eV (maximum value for hole doping) at room temperature. These values are better compared with values of graphene[55] and are comparable to silicene on a graphene substrate (Si_2C_6).[56] While the Seebeck coefficient is nearly constant for pristine TS systems ($\mu - \varepsilon_f = 0.0$), S reaches a maximum value at around 250–300 K for $\mu - \varepsilon_f = \pm 0.05$ (Fig. S6(b), ESI†).

The power factor is another important parameter for the transport properties. The calculated value of the power factor $P = S^2\sigma/\tau$ is shown in Fig. 10c. The variation of power factor with chemical potential is anisotropic. The maximum value of the power factor is higher in the $\mu - \varepsilon_f < 0$ region than with $\mu - \varepsilon_f > 0$, and the obtained value is $9.29 \times 10^{10}\ W\ m^{-1}\ K^{-2}\ s^{-1}$ for $\mu < 0$ ($\mu - \varepsilon_f = -0.063$ eV) at room temperature. The power factor for pristine TS is independent of temperature and is negligible, while for a doped system it rises to a maximum value at around 300 K. It is interesting to note that for a hole-doped system the power factor is higher than the electron-doped system (Fig. S6(c), ESI†).

Finally, we calculated the electronic figure of merit (ZT_{el}) using eqn (12), which is a dimensionless parameter, determining

Table 5 Comparative study of the various thermoelectric properties of few 2D materials at room temperature

Structure [ref.]	σ/τ (Ω^{-1} m^{-1} s^{-1})	S (μV K^{-1})	$S^2\sigma/\tau$ (W m^{-1} K^{-2} s^{-1})	ZT
Graphene[55]	3.30×10^{18}	31	0.03×10^{11}	0.08
Silicene[59]	—	—	—	0.36[a]
Germanene[59]	—	—	—	0.41[a]
Si_2C_6[56]	—	62	—	—
T-germanene[60]	3.16×10^{18}	57	0.44×10^{11}	0.10[a]
Germagraphene[61]	—	309	1.56×10^{11}[b]	—
MoS_2[62]	12.50×10^{18}	550	4.20×10^{11}	0.70
SiC(T2)[17]	4.25×10^{19}	—	—	—
TS [this work]	4.52×10^{19}	73	0.93×10^{11}	0.16[a]

[a] Indicates the electronic figure of merit ZT_{el}. [b] Relaxation time constant has been taken as 10^{-14} s.

Table 6 Calculated values of the various maximum thermoelectric properties of different TSNRs at room temperature

Structure	σ/τ (Ω^{-1} m^{-1} s^{-1})	S (μV K^{-1})	$S^2\sigma/\tau$ (W m^{-1} K^{-2} s^{-1})	ZT_{el}
S-ATSNR $N = 3$	2.28×10^{19}	69.9	0.24×10^{11}	0.192
S-ATSNR $N = 4$	4.93×10^{19}	61.3	0.68×10^{11}	0.251
A-ATSNR $N = 3.5$	2.67×10^{19}	89.6	0.39×10^{11}	0.281
A-ATSNR $N = 4.5$	2.67×10^{19}	67.8	0.72×10^{11}	0.551
ZTSNR $N = 3$	11.2×10^{19}	58.0	0.24×10^{11}	0.13
ZTSNR $N = 4$	2.13×10^{19}	54.7	0.62×10^{11}	0.15
TS [this work]	4.52×10^{19}	73.0	0.93×10^{11}	0.16

the thermoelectric performance of the material and this is shown in Fig. 10d. As a general rule, materials with good thermoelectric components have $ZT \approx 1$. Although large values of ZT have been predicted in a few materials, concerning their practical application and synthesis, however, it is far from reality.[57] Larger values of the Seebeck coefficient and electrical conductivity and a small value of thermal conductivity should lead to a larger ZT. But due to the Weidemann–Franz law, κ_{el}/σ = constant $\times$ T (generally for metals), the increase of any one of these conductivities will lead to the increase of the other.[58] Also, ZT_{el} as given in eqn (12) is not a physically measurable quantity but is still important as it provides the maximum value of the total figure of merit ZT. A small ZT_{el} will always imply a smaller ZT. Our results show that the maximum $ZT_{el} \approx 0.156$ appears at $\mu - \varepsilon_f = -0.063$ eV at room temperature. The figure of merit for $\mu - \varepsilon_f = 0.0$ is nearly zero for all temperatures (Fig. S6(d), ESI†). For $\mu - \varepsilon_f = \pm 0.05$ the figure of merit reaches a maximum at 250 K, with the value ZT_{el} for hole-doped systems being slightly higher than the electron-doped system. With the rise of temperature both the electrical and thermal conductivities increase according to the Weidemann–Franz law, and ZT_{el} is nearly proportional to S^2. The maximum value of ZT_{el} is large compared with graphene,[55] but it is smaller than silicene or germanene.[59] We have compared the thermoelectric properties of a few 2D materials in Table 5. A higher value of the power factor, as well as the figure of merit, suggest that TS will give a better performance when hole-doped with an optimal efficiency around 300–350 K. Based on these values we can conclude that TS can be a better option for its potential application in thermoelectric devices.

4.2 Nanoribbons

The electrical conductivity, Seebeck coefficient, power factor, and figure of merit for the nanoribbons were also studied as a function of chemical potential with temperature as a parameter (Fig. S7–S12, ESI†). We considered nanoribbons of width $N = 3$ and 4 for S-ATSNR and ZTSNR, while $N = 3.5$ and 4.5 for A-ATSNR. The maximum values of these four thermoelectric parameters at room temperature are tabulated in Table 6. The electrical conductivity, Seebeck coefficient, and power factor for the nanoribbons are of the same order as the TS nanosheet. The maximum electrical conductivity of all NRs appears away from the pristine state. Also, the NRs show a large figure of merit at low temperatures (100 K). This suggests that NRs could be suitable for high thermoelectric performance for low-to-room-temperature regions. Among the NRs the power factor of A-ATSNR is higher than that of the comparable width S-ATSNR and ZTSNR, also the higher value of the figure of merit indicates that A-ATSNR exhibits a better thermoelectric performance with appropriate doping.

Our theoretical study of these optical and thermo-electrical properties of the TS nanosheet and TSNRs will surely motivate further research, both theoretical and experimental, synthesis, application, and exploration of other properties. In this respect, we believe that the theoretical results of free-standing T-silicene may be a roadmap for experimentalists. However, similar to silicene, this material needs a metal substrate for its growth during synthesis. The formation energy comparable to silicene, absence of negative phonon modes, and its mechanical and dynamical stability suggest that it may be synthesized in the near future. In ref. 39 the authors suggested a possible route for the synthesis of this material.

5 Conclusion

In summary, we have systematically investigated the optical and thermoelectric properties of the 2D non-hexagonal TS

sheet and nanoribbons using first-principles calculations. The optical properties of these structures are highly anisotropic. The optical properties of the NRs are largely dependent on the edge state and the types of polarization. Strong optical responses are observed in the IR to visible region for incident light of parallel polarization whereas for perpendicular polarization it is in the UV region of the EM spectrum. Calculation of the imaginary part of the dielectric function of the sheet reveals the existence of both π–π^* interband and σ band transitions. Multiple plasma frequencies for the sheet and TSNRs are observed for parallel polarization, which are also confirmed by the EELS peaks. The ATSNR shows strong absorption in the IR and UV regions of the electromagnetic spectrum. The electrical conductivity, the figure of merit, and the power factor of the TS sheet are found to be higher than graphene at room temperature, which suggests TS as a better material for its performance in thermoelectric devices over graphene. The TS sheet will perform better in the hole-doped region than in the pristine or electron-doped region. The figure of merit calculation shows that A-ATSNR provides a better thermoelectric performance than the TS sheet. So the wonderful optical and thermoelectric properties of the TS sheet and its nanoribbons may register them as an obvious choice for present optical, opto-electronics, and thermoelectric devices.

Author contributions

NSM: formal analysis, writing original draft; SN: conceptualization, simulations, formal analysis, writing original draft; DJ: formal analysis, discussions, finalizing manuscript; NKG: finalizing manuscript, discussions.

Conflicts of interest

The authors declare that they have no known competing financial interest or personal relationship that could have appeared to influence the work reported in the paper.

Acknowledgements

NSM and SN thank Arka Bandyopadhyay and Supriya Ghosal, University of Calcutta for stimulating discussions.

References

1 K. S. Novoselov, A. K. Geim, S. V. Morozov, D. Jiang, Y. Zhang, S. V. Dubonos, I. V. Grigorieva and A. A. Firsov, *Science*, 2004, **306**, 666.
2 F. Bonaccorso, Z. Sun, T. Hasan and A. C. Ferrar, *Nat. Photonics*, 2010, **4**, 611.
3 F. Schweirz, *Nat. Nanotechnol.*, 2010, **5**, 487.
4 M. J. Allen, V. C. Tung and R. B. Kaner, *Chem. Rev.*, 2010, **110**(1), 132.
5 A. A. Baladin, *Nat. Mater.*, 2011, **10**, 569.
6 R. Mas-Balleste, C. Gomez-Navarro, J. Gomez-Herrero and F. Zamora, *Nanoscale*, 2011, **3**, 20.
7 A. Gupta, T. Sakthivel and S. Seal, *Prog. Mater. Sci.*, 2015, **73**, 44.
8 Q. Tang and Z. Zhou, *Prog. Mater. Sci.*, 2013, **58**, 1244.
9 L. C. Xu, R. Z. Wang, M. S. Miao, X. L. Wei, Y. P. Chen, H. Yan, W. M. Lau, L. M. Liu and Y. M. Ma, *Nanoscale*, 2014, **6**, 1113.
10 A. Bandyopadhyay, S. Datta, D. Jana, S. Nath and M. M. Uddin, *Sci. Rep.*, 2020, **10**, 2502.
11 H. Wu, Y. Qian, Z. Du, R. Zhu, E. Kan and K. Deng, *Phys. Lett. A*, 2017, **381**, 3754.
12 C. Xu, Y. Wang, R. Han, H. Tu and Y. Yan, *New J. Phys.*, 2019, **21**, 033005.
13 Y. Liu, G. Wang, Q. Huang, L. Guo and X. Chen, *Phys. Rev. Lett.*, 2011, **108**, 225505.
14 P. Mélinon, B. Masenelli, F. Tournus and A. Perez, *Nat. Mater.*, 2007, **6**, 479.
15 T. Susi, V. Skakalova, A. Mittelberger, P. Kotrusz, M. Hulman, T. J. Pennycook, C. Mangler, J. Kotakoski and J. C. Meyer, *Sci. Rep.*, 2017, **7**, 1.
16 S. Chabi and K. Kadel, *Nanomaterials*, 2020, **10**, 2226.
17 M. Houmad, O. Dakir, M. H. Mohammed, M. Khuili, A. E. Kenz and A. Benyoussef, *Chem. Phys. Lett.*, 2020, **754**, 137710.
18 F. Bonaccorso, Z. Sun, T. Hasan and A. C. Ferrari, *Nat. Photonics*, 2010, **4**, 611–622.
19 D. Prezzi, D. Varsano, A. Ruini, A. Marini and E. Molinari, *Phys. Rev. B: Condens. Matter Mater. Phys.*, 2008, **77**, 041404(R).
20 W. Liao, G. Zhou and F. Xi, *J. Appl. Phys.*, 2008, **104**, 126105.
21 V. A. Saroka, M. V. Shuba and M. E. Portnoi, *Phys. Rev. B*, 2017, **95**, 155438.
22 A. Bandyopadhyay, A. Nandy, A. Chakrabarti and D. Jana, *Phys. Chem. Chem. Phys.*, 2017, **19**, 21584.
23 A. Bandopadhyay and D. Jana, *Rep. Prog. Phys.*, 2020, **83**, 056501.
24 A. Bandyopadhyay, S. Paria and D. Jana, *J. Phys. Chem. Solids*, 2018, **123**, 172.
25 J. Deb, D. Paul and U. Sarkar, *J. Phys. Chem. A*, 2020, **124**(7), 1312.
26 S. Nath, A. Bandyopadhyay, S. Datta, M. M. Uddin and D. Jana, *Phys. E*, 2020, **120**, 114087.
27 S. Chowdhury and D. Jana, *Rep. Prog. Phys.*, 2016, **79**, 126501.
28 G. Liu, W. Luo, X. Wang, X. Lei, B. Xu, C. Ouyang and S. Liu, *J. Mater. Chem. C*, 2018, **6**, 5937.
29 S. Cahangirov, M. Topsakal, E. Aktürk, H. Sahin and S. Ciraci, *Phys. Rev. Lett.*, 2009, **102**, 236804.
30 N. J. Roome and J. D. Carey, *ACS Appl. Mater. Interfaces*, 2014, **6**, 7743.
31 K. Chinnathambi, A. Chakrabarti, A. Banerjee and S. K. Deb, Optical Properties of Graphene-like Two Dimensional Silicene, 2012, https://arxiv.org/abs/1205.5099v1.
32 L. Matthes, O. Pulci and F. Bechstedt, *New J. Phys.*, 2014, **16**, 105007.
33 R. John and B. Merlin, *J. Phys. Chem. Solids*, 2017, **110**, 307.

34 A. A. Balandin, S. Ghosh, W. Bao, I. Calizo, D. Teweldebrhan, F. Miao and C. N. Lau, *Nano Lett.*, 2008, **8**, 902.

35 K. Yang, Y. Chen, R. Dâgosta, Y. Xie, J. Zhong and A. Rubio, *Phys. Rev. B: Condens. Matter Mater. Phys.*, 2012, **86**, 045425.

36 K. Yang, S. Cahangirov, A. Cantarero, A. Rudio and R. D'Agosta, *Phys. Rev. B: Condens. Matter Mater. Phys.*, 2014, **89**, 125403.

37 H. Tu, J. Zhanga, Z. Guoa and C. Xu, *RSC Adv.*, 2019, **9**, 42245.

38 H. Alavi-Rad, A. Kiani-Sarkaleh, S. Rouhi and A. Ghadimi, *AIMS Mater. Sci.*, 2020, **6**(6), 1010.

39 N. S. Mondal, S. Nath, D. Jana and N. K. Ghosh, *J. Phys. Chem. Solids*, 2021, **150**, 109801.

40 P. Ordejon, E. Artacho and J. M. Soler, *Phys. Rev. B: Condens. Matter Mater. Phys.*, 1996, **53(R)**, R10441.

41 D. S. Portal, P. Ordejon, E. Artacho and J. M. Soler, *Int. J. Quantum Chem.*, 1997, **65**, 53.

42 J. M. Soler, E. Artacho and A. Garca, *et al.*, *J. Phys.: Condens. Matter*, 2002, **14**, 2745.

43 J. P. Perdew, K. Burke and M. Ernzerhof, *Phys. Rev. Lett.*, 1996, **77**, 3865.

44 N. Troullier and J. L. Martins, *Phys. Rev. B: Condens. Matter Mater. Phys.*, 1991, **43**, 1993.

45 H. J. Monkhorst and J. D. Pack, *Phys. Rev. B: Solid State*, 1976, **13**, 5188.

46 J. P. Perdew and A. Zunger, *Phys. Rev. B: Condens. Matter Mater. Phys.*, 1981, **23**, 5048.

47 S. Datta, P. Singh and D. Jana, *et al.*, *Carbon*, 2020, **168**, 125.

48 S. Datta, P. Singh, C. B. Chaudhuri and D. Jana, *et al.*, *J. Phys.: Condens. Matter*, 2019, **31**, 495502.

49 D. Jana, C. L. Sun, L. C. Chen and K. H. Chen, *Prog. Mater. Sci.*, 2013, **58**, 565.

50 S. Jana, A. Bandyopadhyay and D. Jana, *Phys. Chem. Chem. Phys.*, 2019, **21**, 13795.

51 P. Giannozzi, *et al.*, *J. Phys.: Condens. Matter*, 2009, **21**, 395502.

52 P. Giannozzi, *et al.*, *J. Phys.: Condens. Matter*, 2017, **29**, 465901.

53 G. K. Madsen and D. J. Singh, *Comput. Phys. Commun.*, 2006, **175**, 67.

54 R. Das, S. Chowdhury, A. Majumdar and D. Jana, *RSC Adv.*, 2015, **5**, 41.

55 A. H. Reshak, S. A. Khan and S. Auluck, *J. Mater. Chem. C*, 2014, **2**, 2346.

56 M. A. B. Hamid, C. K. Tim, Y. B. Yaakob and M. A. B. Hazan, *Mater. Res. Express*, 2019, **6**, 055803.

57 R. Venkatasubramanian, E. Siivola, T. Colpitts and B. O'Quinn, *Nature*, 2001, **413**, 597.

58 N. W. Ashcroft and N. D. Mermin, *Solid State Physics*, Saunders College Publishing, Philadelphia, 1976.

59 K. Yang, S. Cahangirov, A. Cantarero, A. Rubio and R. S'Agosta, *Phys. Rev. B: Condens. Matter Mater. Phys.*, 2014, **89**, 125403.

60 S. Ghosal, A. Bandyopadhyay and D. Jana, *Phys. Chem. Chem. Phys.*, 2020, **22**, 19957.

61 S. Datta and D. Jana, *Phys. Chem. Chem. Phys.*, 2020, **22**, 8606.

62 J. Hong, C. Lee, J.-S. Park and J. H. Shim, *Phys. Rev. B*, 2016, **93**, 035445.